Asociación Argentina
de Mecánica Computacional

Mecánica Computacional Vol XLI, pp. 321-331
C.I. Pairetti, M.A. Pucheta, M.A. Storti, C.M. Venier (Eds.)
H. Castro, J. D'Elía, L. Battaglia, M. Coussirat, S. Sarraf, A. Scarabino (Issue eds.)
Rosario, November 5-8, 2024

MODELING DROP ATOMIZATION USING COMPUTATIONAL FLUID DYNAMICS

Patricio Canciani[a,d], **César Pairetti**[a,b] **and Hugo Navone**[a,c]

[a]*Facultad de Ciencias Exactas, Ingeniería y Agrimensura (UNR), Pellegrini 250, Rosario, Santa Fe, Argentina.*

[b]*Sorbonne Université, CNRS, Institu Jean Le Rond d'Alembert, 4 Place Jussieu 75252, Paris, France.*

[c]*Instituto de Física de Rosario (CONICET), Ocampo y Esmeralda, S2000EKF, Rosario, Santa Fe, Argentina.*

[d]*Instituto Balseiro, UNCuyo, Av. Ezequiel Bustillo 9500, San Carlos de Bariloche, Rio Negro, Argentina.*

Keywords: DNS, droplet, Weber, axisymmetric, aerobreakup

Abstract. Atomization, a process in which droplets break into smaller structures, is common in both natural and industrial contexts. The mechanisms of droplet deformation and breakup are often described through hydrodynamic instabilities, informed by experimental studies, theoretical developments, and simulations via Computational Fluid Dynamics (CFD). In this work, Direct Numerical Simulations (DNS) were employed to analyze droplet atomization under various conditions. Two models were considered for studying droplet deformation and breakup: one axisymmetric and the other three-dimensional. The results showed that the deformation and fragmentation of the droplet are highly dependent on the Weber number. Additionally, an increase in the Weber number accelerates the onset of the fragmentation process. The three-dimensional (3D) simulations revealed perforations with a spatial distribution characterized by initial axial symmetry, which dissipates as fragmentation progresses. DNS proves valuable in such studies due to its ability to detect the droplets produced during atomization, enabling the measurement of their positions and velocities at each moment, which can be aggregated into statistical data.

ISSN: 2591-3522 DOI: 10.70567/mc.v41i6.32

1 INTRODUCTION

Atomization is the process in which a liquid mass breaks into smaller droplets; it is also known as aerobreakup when the initial configuration involves a droplet. The number of smaller droplets formed from the breakup of the primary droplet is influenced by the flow conditions and ultimately determines the droplet size distribution (Eggers and Villermaux, 2008; Ling et al., 2017; Villermaux and Bossa, 2009).

Atomization occurs in natural phenomena such as rain (Villermaux and Bossa, 2009), and bubbles and droplets are key players in the heat and mass exchange between the oceans and the atmosphere (Deike, 2022), as well as in volcanic eruptions (Kaminski and Jaupart, 1998). In industrial applications, atomization is critical for fuel spraying within gas turbine combustion chambers (Liu et al., 1993), spray drying of agricultural products (Santos et al., 2018), and powder production (Li and Fritsching, 2017), among many other processes. More recently, the SARS-CoV-2 (Covid-19) pandemic has highlighted the importance of droplet fragmentation in the study of respiratory disease transmission (Pairetti et al., 2021; Sharma et al., 2021).

Droplet atomization occurs when a gas stream deforms a droplet to the point of fragmentation, producing multiple smaller droplets. This process results from the formation and rupture of liquid sheets driven by Rayleigh-Taylor or Kelvin-Helmholtz instabilities. The Weber number primarily governs the fragmentation process, with distinct breakup modes corresponding to its value (Theofanous and Li, 2008). Rayleigh-Taylor Piercing (RTP) modes occur for $\mathrm{We} < 100$, while Shear Induced Entrainment (SIE) modes appear for $\mathrm{We} > 1000$, with a transitional range between $100 < \mathrm{We} < 1000$.

A robust experimental foundation is essential to support and validate theoretical findings. In this context, numerous experimental studies have been conducted (Faeth et al., 1995; Chou and Faeth, 1998; Theofanous et al., 2004; Liu and Reitz, 1997; Zhao et al., 2010; Opfer et al., 2014; Jackiw and Ashgriz, 2021). These studies have identified various deformation and breakup regimes based on different flow conditions (Nicholls and Ranger, 1969; Pilch and Erdman, 1987; Guildenbecher et al., 2009).

However, for many practically relevant flows, the involved length scales are small, time scales are short, and optical access to much of the flow is limited. This makes Computational Fluid Dynamics (CFD) essential for developing numerical strategies to solve the equations governing these complex processes. Direct Numerical Simulation (DNS) specifically uses numerical methods to solve the fundamental equations of fluid mechanics, providing approximate values for velocities and flow properties in space. With the increase in computational power over recent decades, DNS has become increasingly common for analyzing droplet deformation and breakup processes under various flow conditions (Zaleski et al., 1995; Han and Tryggvason, 1999; Feng, 2010; Kékesi et al., 2014; Jain et al., 2015, 2019; Mahmood and Ling, 2021).

The process of liquid atomization has been studied for decades due to its numerous applications. The primary goal of these studies is to understand the properties of the sprays (droplet clouds) generated by atomization. Understanding the dynamics of this process is crucial for designing, implementing, and evaluating models that predict the final droplet size. One of the key reasons for studying atomization is to determine the conditions that produce fragment sizes appropriate for the intended application. A thorough understanding of the fragmentation process is essential for estimating the droplet size distribution, which in turn determines the surface/volume ratio and the efficiency of various physicochemical processes.

2 MODELING AND STUDY OF THE PROBLEM

2.1 Description of the Physical System

The system under study consists of a spherical droplet, initially at rest, with an initial diameter D_o, and with density ρ_l and viscosity μ_l. It is submerged in a gas stream with density ρ_g and viscosity μ_g. The velocity of the gas stream is U_o. The surface tension coefficient at the liquid-gas interface is represented by σ.

A single-fluid formulation is used for the numerical simulations (Tryggvason et al., 2011). The flow properties are computed based on the volume fraction f using arithmetic or harmonic means. These means are also employed to calculate the average mixture properties (Ishii, 1975; Tryggvason et al., 2011), such as the quantity ρ (arithmetic mean) and the quantity μ (harmonic mean).

$$\rho(f) = \rho_l\, f + \rho_g\,(1-f) \quad ; \quad \mu(f) = \left(\frac{f}{\mu_l} + \frac{1-f}{\mu_g}\right)^{-1} \tag{1}$$

The governing differential equations for the coupled liquid-gas flow are presented in Equation (2). The first equation is the continuity equation, which indicates that both the droplet liquid and the surrounding gas are incompressible. The second equation corresponds to the conservation of momentum, which is the Navier-Stokes equation. The last one is related to the evolution of the interface, expressed as an advection equation in terms of the volume fraction f.

$$\begin{gathered} \nabla^* \cdot \mathbf{u}^* = 0 \\ \tfrac{\rho^* f + (1-f)}{\sqrt{\rho^*}} \left[\tfrac{\partial \mathbf{u}^*}{\partial t^*} + \sqrt{\rho^*}\,\mathbf{u}^* \cdot \nabla^* \mathbf{u}^*\right] = -\nabla^* \mathrm{p}^* + \\ + \tfrac{\mu^*}{f + \mu^*(1-f)} \tfrac{1}{\mathrm{Re}} \nabla^{*2} \mathbf{u}^* + \tfrac{1}{\mathrm{We}}\, \kappa^* \delta_S^*\, \mathbf{n} \\ \tfrac{\partial f}{\partial t^*} + \sqrt{\rho^*}\,\mathbf{u}^* \cdot \nabla^* f = 0 \end{gathered} \tag{2}$$

The description and characterization of the two-phase flow are conducted using four dimensionless parameters (Theofanous et al., 2004; Jain et al., 2015; Guildenbecher et al., 2009):

$$\mathrm{We} = \frac{\rho_g D_o {U_o}^2}{\sigma}; \quad \mathrm{Re} = \frac{\rho_g D_o U_o}{\mu_g}; \quad \rho^* = \frac{\rho_l}{\rho_g}; \quad \mu^* = \frac{\mu_l}{\mu_g} \tag{3}$$

The equations in (2) are made dimensionless using the initial diameter D_o and the inlet velocity U_o. Similarly, the physical time t is made dimensionless using the characteristic time scale of Nicholls and Ranger (Nicholls and Ranger, 1969), $t^* = t/t_c$, where the time scale t_c is defined in equation (4).

$$t_c = \frac{D_o}{U_o}\sqrt{\rho^*} \tag{4}$$

2.2 Computational Modeling Platform and Numerical Methods

In this work, the development platform Basilisk (Popinet, 2014) is used to perform DNS simulations of multiphase flows, employing the Finite Volume Method along with the projection method, with spatial discretization using adaptive quadtree meshes. Adaptive Mesh Refinement

(Popinet, 2009) optimizes the resolution in areas of greater interest. The interface is captured using the Volume Of Fluid methodology with the PLIC[1] approximation (Popinet, 2009; Tryggvason et al., 2011). Although this approach is computationally expensive, its application is necessary to accurately represent all the scales involved in such complex phenomena.

2.3 Axisymmetric and Three-Dimensional Models

The domain's dimensions and the initial position of the droplet are chosen to ensure that boundary effects do not significantly influence the fragmentation process. Two-dimensional-axisymmetric (2D-axisymmetric) and three-dimensional (3D) simulations are performed with their computational domains schematically shown in Figure 1. In both configurations, the gas enters the domain from the left face, normal to it, with a uniform velocity U_o. On this same face, a Neumann boundary condition equal to zero is imposed on the pressure field to allow it to adjust according to the evolution of the variables in the simulation domain. On the right face, the pressure field is fixed at zero, with a Neumann boundary condition of zero imposed on the normal component of the velocity to ensure mass conservation. On the rest of the domain boundaries, free-slip conditions are adopted.

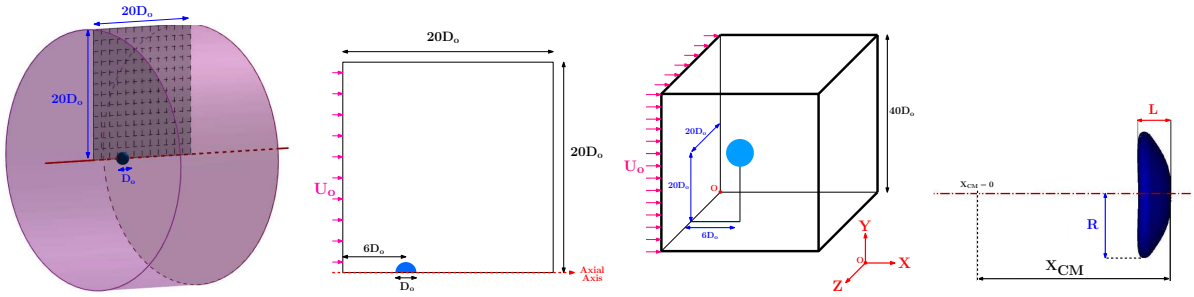

(a) (b) (c) (d)

Figure 1: Problem Schemes. (a) 3D domain of the axisymmetric configuration. (b) 2D-axisymmetric domain. (c) Cubic domain with side $40D_o$ for the 3D simulations. (d) Radial evolution R, longitudinal deformation L, and position X_{CM} of the droplet's center of mass. (Image extracted and modified from Pairetti et al. (2018)).

Table 1 lists the range of parameters covered in this work. For all cases, the relative viscosity value is $\mu^* = 100$. Values for Re, We, and ρ^* were selected based on the literature and areas of interest. For the relative density, values close to those of a water droplet submerged in an air stream ($\rho^* = 833.3$) and those of an iso-octane droplet submerged in a nitrogen stream ($\rho^* = 188.3$) were considered, as well as intermediate values for the analysis.

	2D-Axisymmetric	**3D**
$\boldsymbol{\rho^*}$	30, 200, 500, 1000	30, 200, 500
Re	500	500
We	10, 20, 40	20, 40

Table 1: Dimensionless parameters selected for this work.

[1]Piecewise Linear Interface Calculation

3 RESULTS

3.1 Validation of the Numerical Tool

Figure 2a illustrates the temporal evolution of the radius for an axisymmetric simulation with Re $= 2180$, We $= 15$, $\rho^* = 20$, and $\mu^* = 90.9$. The resulting curve is compared with the results of a simulation by Marcotte and Zaleski (2019). The reference study uses a mesh resolution of $\Delta/D_o = 0.00125$, while in our work, the highest resolution simulation corresponds to $\Delta/D_o = 0.005$.

Figure 2b shows the temporal evolution of the droplet radius for a simulation with Re $=$ 400, We $= 15$, $\rho^* = 20$, and $\mu^* = 90.9$ from the work of Mahmood and Ling (2021). The authors use a mesh resolution of $\Delta/D_o = 0.004$. Additionally, the normalized Kolmogorov scale is $\eta/\mathrm{D_o} \simeq 0.0025$, so to capture the smallest scales, η/D_o must be greater than Δ/D_o. Considering these factors and the reference data, the behavior of our simulations is deemed acceptable.

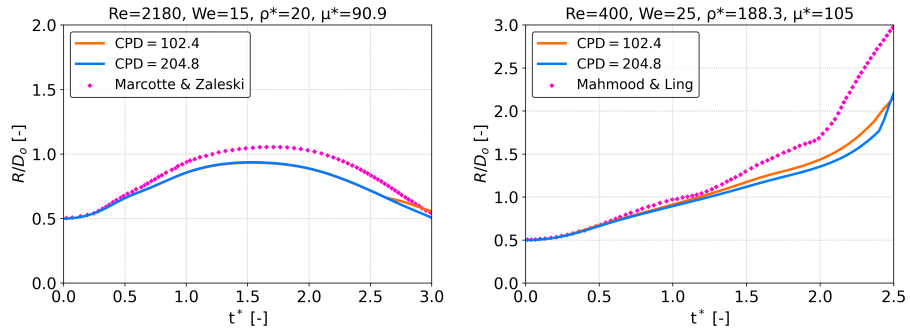

(a) (b)

Figure 2: Simulations performed for the validation of the numerical tool. The mesh resolution is characterized by CPD (Cells Per Diameter).

3.2 2D-Axisymmetric Simulations

Axisymmetric simulations are conducted considering Re $= 500$ and various combinations of We and ρ^*. Figure 3 provides a summary of these simulations and shows snapshots of the gas-liquid interface of the droplet. It can be observed that fragmentation does not occur regardless of the density value when the Weber number is low (We $= 10$). However, at higher values, different modes of droplet stretching and fragmentation are observed. Fragmentation occurs in cases with $\rho^* \geq 200$, We $= 20$, and We $= 40$. In the first case, the breakup time falls within the range $1.87 < t_b^* < 2.20$, and in the second case, it falls within the range $1.57 < t_b^* < 1.87$.

These observations are consistent with the temporal evolution of the droplet radius (Figure 4). At We $= 10$, the droplet's radius increases and then returns to its original value. On the other hand, an increase in the Weber number results in a more pronounced expansion or stretching of the droplet, occurring in a shorter time.

3.3 3D Simulations

From the simulations conducted with the axisymmetric model, it is observed that aerosol production cases require high values of We. Since droplet fragmentation occurs at the threshold

value $\rho^* = 200$, only values of $\rho^* = 30, 500$ are considered. Due to the computational cost of the calculations, only simulations with $\mathrm{Re} = 500$ are included.

(a)

Figure 3: Deformation and breakup of droplets for relative viscosity $\mu^* = 100$, $\mathrm{Re} = 500$, and different values of We and ρ^*.

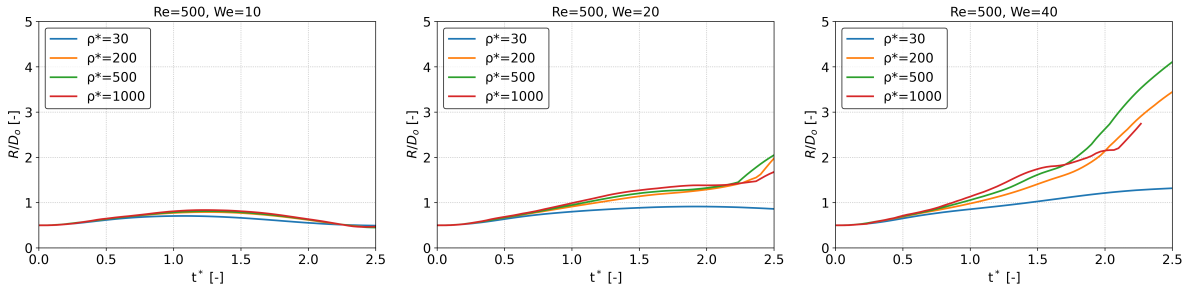

Figure 4: (a) Temporal evolution of the radius for $\mu^* = 100$, $\mathrm{Re} = 500$, and different values of We and ρ^*.

Figure 5 shows the temporal evolution of the radius. The droplet with lower density exhibits

a slight expansion and reduction in its radius, which is similar to the results obtained with the axisymmetric model. It is important to note that the change in slopes corresponds to the onset or development of the droplet fragmentation process. In cases where fragmentation occurs, the "radius" R refers to the radius of the cloud formed by the resulting smaller droplets.

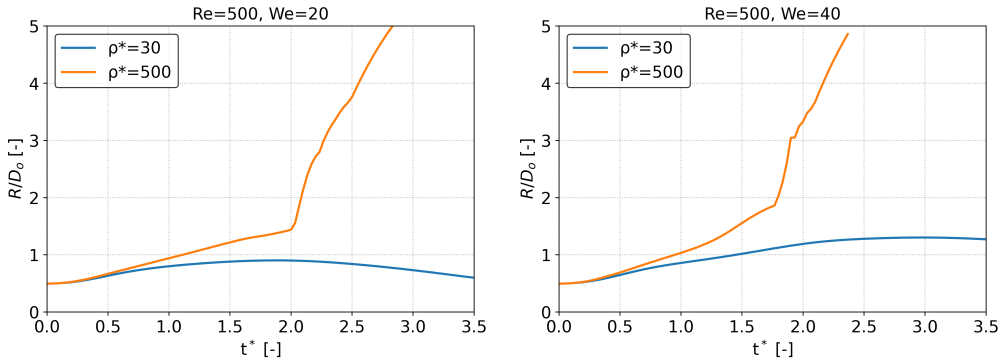

(a) (b)

Figure 5: Temporal evolution of the radius with $\mu^* = 100$.

3.4 2D-Axisymmetric Simulations vs 3D Simulations

2D-axisymmetric simulations allow for modeling the three-dimensional problem at the computational costs of 2D simulations. This approach significantly reduces the computational cost of droplet simulations. As shown in Figure 6, the models are completely consistent for small densities. This indicates that for low relative density values and moderate Reynolds numbers, computational savings can be achieved by using 2D-axisymmetric simulations.

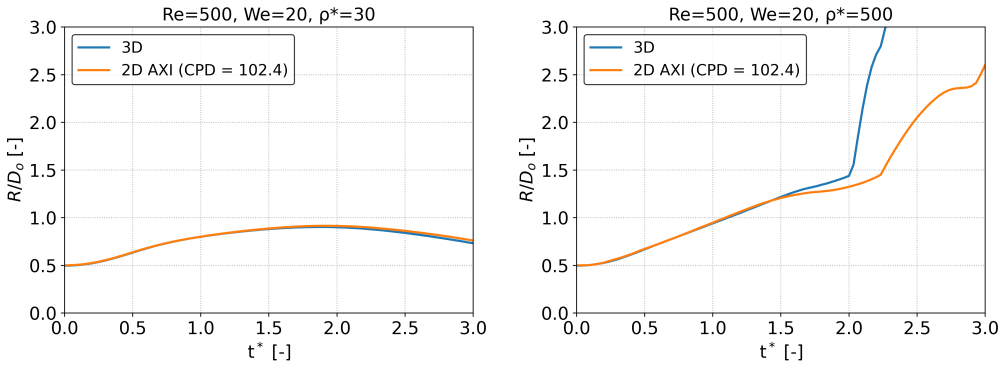

(a) (b)

Figure 6: Comparison between the 2D-axisymmetric model and the 3D model.

For larger densities, partially consistent results are observed, with discrepancies arising near the development of instabilities leading to fragmentation.

3.5 Atomization Statistics (3D Results)

The use of DNS as a strategy to study the aerobreakup phenomenon allows for the estimation of certain physical quantities. Figure 7a shows the volume fraction as a function of the Sauter

Mean Diameter (SMD)[2] for four different time instances. On the other hand, Figure 7b displays the histogram of the number of droplets associated with a certain SMD for the same four time instances.

Snapshots of the droplet corresponding to these time instances are shown in Figure 8. At $t^* = 2$, a few droplets are observed due to perforations, consistent with the observed number of droplets. The volume fraction of these droplets is small for these diameter values. At $t^* = 2.5$, the holes expand until the ligaments connecting the center to the edge break into small droplets with a slightly larger mean diameter, and therefore, their volume fraction is also higher. Between $t^* = 2.5$ and $t^* = 3$, the edge deforms and undergoes pinch-off[3]. Due to the larger diameter of the edge ligament, the fragmentation process takes longer to manifest. Finally, at $t^* = 3.5$, the edge breaks into droplets of various sizes, resulting in a 'shift' to the right of the magenta curve in Figure 7a, indicating a more uniform size distribution.

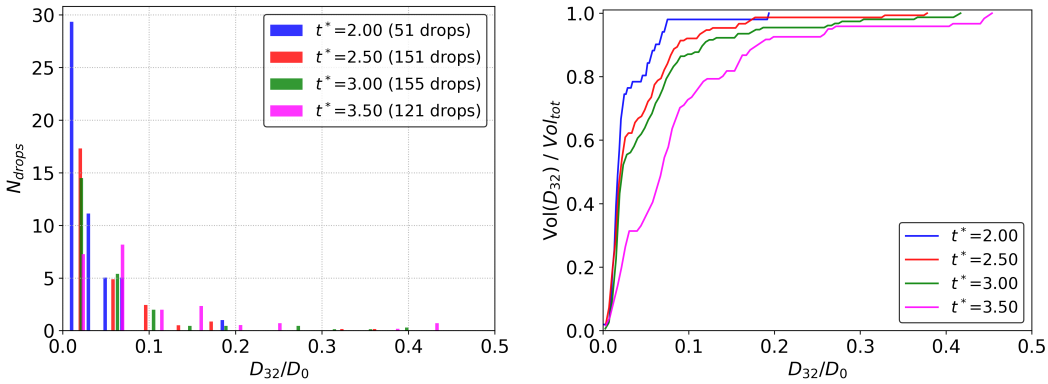

(a) (b)

Figure 7: (a) Histogram of the number of droplets associated with their Sauter diameter for different time instances. (b) Volume fraction as a function of the SMD for different time instances. Results from a simulation with Re $= 500$, We $= 20$, and $\rho^* = 500$.

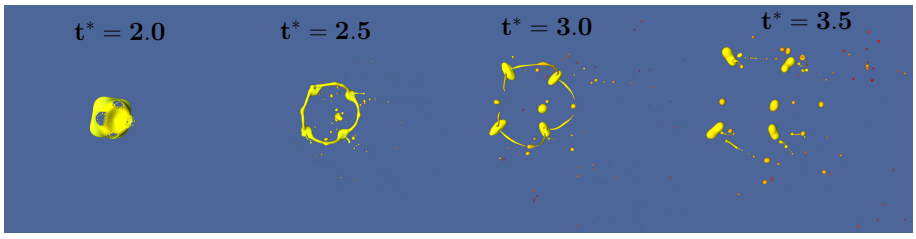

(a)

Figure 8: Snapshots of the droplet evolution for different time instances. Results from a simulation with Re $= 500$, We $= 20$, and $\rho^* = 500$.

[2]The Sauter Mean Diameter (SMD) quantifies the volumetric area density of a droplet. During its deformation, the SMD decreases as the surface area increases but may recover or increase if the droplet is pierced or fragmented.

[3]Narrowing of a specific section until the liquid ligament breaks.

4 CONCLUSIONS

This work explored the problem of aerobreakup and its significance in both natural phenomena and industrial processes. The process of droplet fragmentation is extremely complex.

The computational models were validated by analyzing the temporal evolution of the droplet radius through direct numerical simulations in an axisymmetric configuration, comparing the results with reference data. This configuration was also used to detect the effects of varying relative density during the droplet deformation stage, prior to breakup, and was compared with three-dimensional simulations.

Comparison between the 2D-axisymmetric and 3D models suggests that axisymmetric simulations are valid for studying deformation, while 3D simulations are necessary to represent turbulence-related physical processes.

DNS provides access to a dataset that, when the simulation fidelity closely matches that of a real experiment, enables a more detailed analysis of the fundamental aspects of the atomization process and the development of predictive models for droplet size-something not achievable through experimentation alone. However, it is important to note that such simulations are computationally expensive, underscoring the need to develop more efficient numerical methods that allow for higher-resolution mesh refinements.

The significance of using DNS in these problems lies in its ability to detect each droplet produced throughout the atomization process, measuring their position and velocity at each moment. This information can be condensed into statistics that allow for comparing both the properties of the resulting spray and the dynamics that generate it.

DNS plays a key role as a complement to experiments, offering a clear advantage by providing condensed and valuable information, such as droplet counts and mean diameters, which are essential for industrial processes. Nonetheless, to fully harness the potential of DNS, advancements in computational efficiency are critical to enable even more refined simulations without prohibitive costs.

REFERENCES

Chou W.H. and Faeth G. Temporal properties of secondary drop breakup in the bag breakup regime. *International journal of multiphase flow*, 1998.

Deike L. Mass transfer at the ocean–atmosphere interface: the role of wave breaking, droplets, and bubbles. *Annual Review of Fluid Mechanics*, 2022.

Eggers J. and Villermaux E. Physics of liquid jets. *Reports on progress in physics*, 2008.

Faeth G., Hsiang L.P., and Wu P.K. Structure and breakup properties of sprays. *International Journal of Multiphase Flow*, 1995.

Feng J.Q. A deformable liquid drop falling through a quiescent gas at terminal velocity. *Journal of Fluid Mechanics*, 2010.

Guildenbecher D., López-Rivera C., and Sojka P. Secondary atomization. *Experiments in Fluids*, 2009.

Han J. and Tryggvason G. Secondary breakup of axisymmetric liquid drops. i. acceleration by a constant body force. *Physics of Fluids*, 1999.

Ishii M. Thermo-fluid dynamic theory of two-phase flow. *NASA STI/Recon Technical Report A*, 1975.

Jackiw I.M. and Ashgriz N. On aerodynamic droplet breakup. *Journal of Fluid Mechanics*, 2021.

Jain M., Prakash R.S., Tomar G., and Ravikrishna R. Secondary breakup of a drop at moderate weber numbers. *Proc. R. Soc. A*, 2015.

Jain S.S., Tyagi N., Prakash R.S., Ravikrishna R., and Tomar G. Secondary breakup of drops at moderate weber numbers: Effect of density ratio and reynolds number. *International Journal of Multiphase Flow*, 2019.

Kaminski E. and Jaupart C. The size distribution of pyroclasts and the fragmentation sequence in explosive volcanic eruptions. *Journal of Geophysical Research: Solid Earth*, 1998.

Kékesi T., Amberg G., and Wittberg L.P. Drop deformation and breakup. *International Journal of Multiphase Flow*, 2014.

Li X.g. and Fritsching U. Process modeling pressure-swirl-gas-atomization for metal powder production. *Journal of Materials Processing Technology*, 2017.

Ling Y., Legros G., Popinet S., and Zaleski S. Direct numerical simulation of an atomizing biodiesel jet: Impact of fuel properties on atomization characteristics. In *Ilass Europe. 28th european conference on Liquid Atomization and Spray Systems*. Editorial Universitat Politècnica de València, 2017.

Liu A.B., Mather D., and Reitz R.D. Modeling the effects of drop drag and breakup on fuel sprays. *SAE Transactions*, 1993.

Liu Z. and Reitz R. An analysis of the distortion and breakup mechanisms of high speed liquid drops. *International journal of multiphase flow*, 1997.

Mahmood T. and Ling Y. Effect of reynolds number on aerobreakup of small liquid drops. In *ICLASS 2021, 15th Triennial International Conference on Liquid Atomization and Spray Systems, Edinburgh, UK*. 2021.

Marcotte F. and Zaleski S. Density contrast matters for drop fragmentation thresholds at low ohnesorge number. *Physical Review Fluids*, 2019.

Nicholls J. and Ranger A. Aerodynamic shattering of liquid drops. *Aiaa Journal*, 1969.

Opfer L., Roisman I., Venzmer J., Klostermann M., and Tropea C. Droplet-air collision dynamics: Evolution of the film thickness. *Physical Review E*, 2014.

Pairetti C., Popinet S., Márquez Damián S., Nigro N., and Zaleski S. Bag mode breakup simulations of a single liquid droplet. In ECCOMAS, editor, *ECCM-ECFD 2018*. University of Glasgow, University of Edinburg, 2018.

Pairetti C., Villiers R., and Zaleski S. A numerical cough machine. *arXiv*, 2021.

Pilch M. and Erdman C. Use of breakup time data and velocity history data to predict the maximum size of stable fragments for acceleration-induced breakup of a liquid drop. *International journal of multiphase flow*, 1987.

Popinet S. An accurate adaptive solver for surface-tension-driven interfacial flows. *Journal of Computational Physics*, 2009.

Popinet S. The Basilisk Code. 2014.

Santos D., Maurício A.C., Sencadas V., Santos J.D., Fernandes M.H., and Gomes P.S. Spray drying: an overview. *Biomaterials-physics and chemistry-new edition*, 2018.

Sharma S., Pinto R., Saha A., Chaudhuri S., and Basu S. On secondary atomization and blockage of surrogate cough droplets in single-and multilayer face masks. *Science advances*, 2021.

Theofanous T. and Li G. On the physics of aerobreakup. *Physics of fluids*, 2008.

Theofanous T., Li G., and Dinh T.N. Aerobreakup in rarefied supersonic gas flows. *J. Fluids Eng.*, 2004.

Tryggvason G., Scardovelli R., and Zaleski S. *Direct numerical simulations of gas–liquid multiphase flows*. Cambridge University Press, 2011.

Villermaux E. and Bossa B. Single-drop fragmentation determines size distribution of rain-

drops. *Nature physics*, 2009.

Zaleski S., Li J., and Succi S. Two-dimensional navier-stokes simulation of deformation and breakup of liquid patches. *Physical review letters*, 1995.

Zhao H., Liu H.F., Li W.F., and Xu J.L. Morphological classification of low viscosity drop bag breakup in a continuous air jet stream. *Physics of Fluids*, 2010.